

## 基于驱动电压自适应调节的弹光调制

梁振坤<sup>1,2,3</sup>, 李晓<sup>1</sup>, 王志斌<sup>1,2,3\*</sup>, 李克武<sup>1,2,3</sup>, 臧晓阳<sup>1,2,3</sup><sup>1</sup>中北大学电气与控制工程学院, 山西 太原 030051;<sup>2</sup>中北大学前沿交叉科学研究院, 山西 太原 030051;<sup>3</sup>中北大学南通智能光机电研究院, 江苏 南通 226000

**摘要** 弹光调制技术以调制精度高、效率高以及光谱范围宽等优势,应用于光通信、偏振分析、光谱分析等诸多领域,然而弹光调制器(PEM)作为一种高品质因数的热-机-电耦合谐振器件,在高压谐振状态下,其谐振频率会随着温度变化发生严重偏移,从而导致驱动效率与调制效率降低。根据弹光调制器的振动模型,分析了导致弹光调制器温漂的影响因素,提出了基于调制信号跟踪和幅值调节的弹光调制器闭环驱动控制方法,通过测试验证了入射光波长为 632.8 nm 时半波与 1/4 波状态下的稳定控制,半波状态下的相位调制幅值精度达到 0.82%,1/4 波状态下的相位调制幅值精确度达到 0.44%。

**关键词** 测量; 相位调制; 弹光调制器; 数字锁相技术; 温漂模型; 反馈控制

中图分类号 TN249

文献标志码 A

doi: 10.3788/CJL202148.1104001

## 1 引言

弹光调制器的基本原理是弹光效应,利用压电晶体给各向异性晶体提供外部机械力,使其产生双折射,该器件是一种热机电耦合器件,在工作过程中通过给压电晶体垂直方向提供高压正弦波信号,使压电晶体在水平方向上产生振动,振动传导至弹光晶体使接收到的入射线偏振光产生相互垂直的两束偏振光,从而实现入射光的相位调制<sup>[1-4]</sup>。

弹光调制器工作时,其产生的相位调制幅值会随着高压驱动电路输出的驱动电压幅值呈正相关变化。但是在驱动电压幅值与相位调制幅值上升的同时,构成弹光调制器的压电石英与硒化锌晶体会在机械振动时产生热损耗,致使谐振频率发生偏移,导致光程差很难在长时间内保持一致,从而降低了弹光调制器的稳定性和调制效率。目前,根据本质原理的不同,调制控制技术分 3 类:1)基于功率监测的偏置点稳定控制技术;2)基于扰动信号的偏置点稳定控制技术;3)基于相位监测的偏置点稳定控制技术。本文在基于相位监测的控制技术的原理上,提

出一种基于现场可编程门阵列(FPGA)的驱动电压自适应调节方法,采用数字频率合成器(DDS)技术控制弹光调制器工作时的方波信号,并采用数字锁相技术来采集电压反馈信号与相位调制信号,以提供弹光调制器的实时工作状态,从而为闭环控制提供数据源。经运算后,将计算值与设定的相位调制幅值进行比较,再通过调节输出方波时钟信号的占空比( $D$ )来调节输出电压幅值,以使得弹光调制器在谐振状态下以设定的参数保持稳定工作,该方法具有精确度高、稳定度高、反馈速度快的特点。

## 2 理论分析

## 2.1 弹光调制器稳定性影响因素分析

弹光调制器在调制过程中产生的相位差即为弹光调制器的可变相位调制幅值。本设计中弹光晶体采用硒化锌(ZnSe)单晶材料,两侧各粘合两块具有逆压电效应的压电石英晶体,压电晶体在高压驱动电路输出的高压正弦信号的作用下会产生伸缩振动,对粘合在一起的弹光晶体形成挤压与拉伸两种作用力,促使弹光晶体也进行长度伸缩振动。振动模式如图 1

收稿日期: 2020-11-05; 修回日期: 2020-11-10; 录用日期: 2020-12-14

基金项目: 装备发展部预研项目、山西省青年科学基金(201901D211234)、山西省自然科学基金(201901D111145)

\*E-mail: wangzhibin@nuc.edu.cn

所示<sup>[5]</sup>。选用的  $x$  切型压电石英晶体不仅可减小谐振状态下热耗散对系统的影响,还可以保证高驱动效率,以便获取尽可能大的调制光程差。

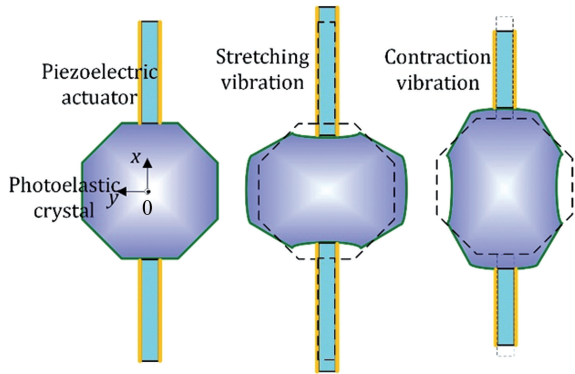


图 1 弹光调制器振动模型  
Fig. 1 Vibration model of PEM

弹光调制器从电学角度来看,是一种品质因数高达  $10^3$  的低阻尼器件<sup>[6]</sup>。虽然弹光调制器是低阻尼器件,但仍会不可避免地产生热耗散,尤其是在采用高压驱动信号来驱动压电石英伸缩时,弹光调制器整体因自身应变幅度的增大而引起的热耗散现象就会变得更加显著。在振动调制过程中因热耗散产生的能量,一部分以热交换方式与环境进行交互,另一部分则会引起弹光调制器自身温度的逐渐升高,进而引起频率匹配条件发生变化,驱动效率也会下降。构建的弹光调制器的动态热交换模型如图 2 所示<sup>[7]</sup>。

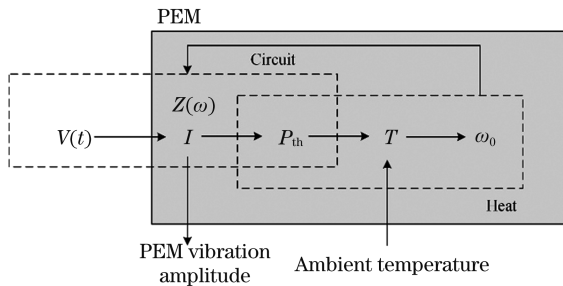


图 2 弹光调制器动态热交换模型  
Fig. 2 Dynamic heat exchange model of PEM

在研究过程中,整个弹光调制器可等效为 RLC 耦合器件。在驱动信号  $V$  的作用下,弹光调制器的热耗散功率取决于品质因数  $Q$ 、谐振电抗  $Z(\omega)$  和依赖于温度的谐振频率  $\omega_r$ 。谐振电抗  $Z(\omega)$  的表达式为<sup>[8]</sup>

$$Z(\omega) = R \left[ 1 + jQ \left( \frac{\omega}{\omega_r} - \frac{\omega_r}{\omega} \right) \right], \quad (1)$$

对应的热损耗功率为

$$P_{th} = \frac{V^2}{R \left[ 1 + Q^2 \left( \omega/\omega_r - \omega_r/\omega \right)^2 \right]}, \quad (2)$$

式中: $V$  为驱动电压幅值; $R$  为弹光调制器的等效阻抗; $Q$  为品质因数; $\omega$  为弹光调制器的高压交流信号角频率<sup>[9-10]</sup>。

当 PEM 在驱动电压  $V$  的作用下和周围环境达到热平衡状态后,弹光调制器的自身温度和谐振频率将不再发生变化。在驱动电压  $V$  的作用下,基于等效谐振电路和热交换模型,得到热耗散引起的弹光调制器的温漂模型为

$$\frac{dT}{dt} = \frac{T_{amb} - T}{\tau_{th}} + \frac{V}{2cR \left[ 1 + Q^2 \left( \frac{\omega}{\omega_r} - \frac{\omega_r}{\omega} \right)^2 \right]}, \quad (3)$$

式中: $c$  为比热容; $R_{th}$  为各部分与环境温度之间的热阻抗; $\tau_{th} = R_{th} \cdot c$  为热时间常数; $T_{amb}$  为环境温度; $T$  为 PEM 自身的温度。

根据弹光调制器的温漂模型,可知因自身谐振或环境温度变化,其谐振频率会发生变化,从而导致驱动效率下降,调制效率同比下降,相位调制幅值也会降低,此时需要加入反馈来实时精确调节驱动电压  $V$  以匹配其他参量的变化,从而保证弹光调制器的稳定工作。为了掌握弹光调制器实时的工作状态,本文采用基于 FPGA 的数字锁相技术来精确追踪调制信号的实时变化,具体的光学系统如图 3 所示<sup>[11-15]</sup>。

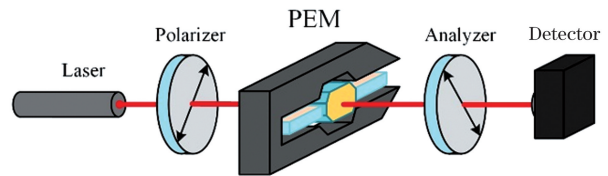


图 3 系统光路示意图  
Fig. 3 Diagram of system light path

在上述光路中,运用 Stokes 参量和 Muller 矩阵进行推算,以便进行具体分析。图 3 中经过  $45^\circ$  的起偏器的入射光信号  $S_{in}$  为<sup>[16]</sup>

$$S_{in} = I_0 [1 \ 0 \ 1 \ 0]^T, \quad (4)$$

式中: $I_0$  为起偏器后的激光光强。弹光调制器的 Muller 矩阵  $M_{PEM}$  为<sup>[17]</sup>

$$M_{PEM} = \begin{bmatrix} 1 & 0 & 0 & 0 \\ 0 & 1 & 0 & 0 \\ 0 & 0 & \cos \delta & \sin \delta \\ 0 & 0 & -\sin \delta & \cos \delta \end{bmatrix}, \quad (5)$$

式中: $\delta$  是 PEM 的时变相位延迟。

$-45^\circ$  的检偏器的穆勒矩阵  $M_A$  为

$$M_A = \frac{1}{2} \begin{bmatrix} 1 & 0 & -1 & 0 \\ 0 & 0 & 0 & 0 \\ -1 & 0 & 1 & 0 \\ 0 & 0 & 0 & 0 \end{bmatrix}. \quad (6)$$

入射光经过图 3 所示的光路系统后, 出射偏振光的 Stokes 参量为<sup>[18]</sup>

$$S_{out} = M_A M_{PEM} S_{in} = \frac{I_0}{2} \begin{bmatrix} 1 - \cos \delta \\ 0 \\ 1 - \cos \delta \\ 0 \end{bmatrix}, \quad (7)$$

其中  $\delta$  可表示为<sup>[19-21]</sup>

$$\delta = \delta_0 \sin(2\pi f_0 t), \quad (8)$$

式中:  $\delta_0$  是相位调制幅值,  $\delta_0 = \frac{2\pi d}{\lambda} k V_m$ ;  $f_0$  是 PEM

的调制频率;  $k$  为弹光晶体的应力光学常数;  $V_m$  为驱动电压峰-峰值;  $d$  为弹光晶体的厚度;  $\lambda$  为入射光的波长。探测器信号为

$$I = \frac{I_0}{2} [1 - \cos(\delta_0 \sin \omega t)]. \quad (9)$$

将(9)式通过贝塞尔级数展开得<sup>[22]</sup>

$$I = \frac{K I_0}{2} [1 - J_0(\delta_0)] - \frac{K I_0}{2} [-2J_2(\delta_0) \cos(2\omega t) - 2J_4(\delta_0) \cos(4\omega t)], \quad (10)$$

式中:  $J_0(\delta_0)$ 、 $J_2(\delta_0)$ 、 $J_4(\delta_0)$  分别为 0, 2, 4 级贝塞尔函数;  $K$  表示第一偏振片后光学系统的传输效率常数, 由探测器输出表达式得出, 探测器输出信号包括直流分量和偶次谐波分量。而采用数字锁相技术可以得到输入信号的所有分量, 本研究仅需要得到相位调制幅值  $\delta_0$ , 因此只需要得到二次谐波分量和四次谐波分量的幅值比值  $J_4/J_2$ , 即可消除无关分量。经运算处理后, 得到的结果如图 4 所示<sup>[23]</sup>。

根据(8)式, PEM 的相位调制幅值与谐振频率和驱动电压峰-峰值有关, 故可以通过调节频率或驱

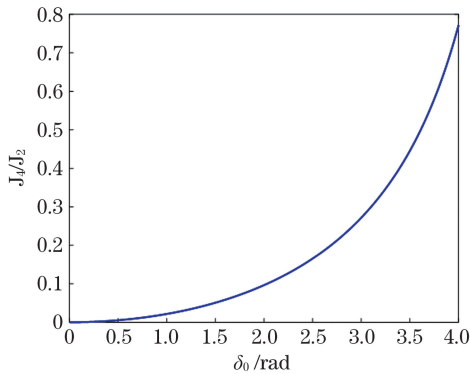


图 4  $J_4/J_2$  随  $\delta_0$  的变化

Fig. 4  $J_4/J_2$  varying with  $\delta_0$

动电压峰-峰值来调节相位调制幅值。本文通过调节驱动电压峰-峰值来调控相位调制幅值, 采用数据锁相的结果来实时跟踪弹光调制器的相位调制幅值, 从而为调节驱动电压提供数据源。

## 2.2 闭环控制系统设计

驱动弹光调制器工作时, 首先将弹光调制器调至谐振状态, 再相应地调节占空比, 从而改变驱动电路的供电电压。令弹光调制器工作在设定的相位调制幅值范围内, 但工作一段时间后, 弹光调制器的谐振频率会在热效应作用下发生偏移, 对应的相位调制幅值也会发生变化, 工作状态无法稳定。为了保证弹光调制器工作的稳定性, 设计了基于数字锁相技术的占空比闭环控制方法, 如图 5 所示。

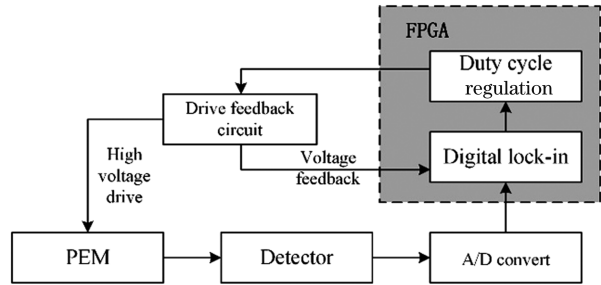


图 5 占空比闭环控制系统

Fig. 5 Duty cycle closed loop control system

图 6 为占空比闭环控制方法的具体实现过程。首先, 由基于 FPGA 的 DDS 模块输出谐振频率处占空比固定的方波信号以为高压驱动电路提供驱动源, 由经 LC 匹配电路处理后产生的高压正弦波驱动弹光调制器工作。入射光经弹光调制器的调制后被探测器接收, 并将光信号转换为电信号, 电信号经 AD 采样模块传入 FPGA 中, 运用数字锁相技术, 将采集信号与存储器中的二倍频、四倍频正余弦参考信号分别进行乘累加运算, 并求得四倍频信号与二倍频信号的比值, 该值与相位调制幅值对应。接下来, 根据每个周期四倍频信号与二倍频信号的比值来实时调节占空比, 当在下一个周期得到的比值小于上一个周期的比值, 增加占空比, 反之则减小占空比, 最终使相位调制幅值始终稳定于固定范围。

## 3 实验验证与数据分析

为了分析弹光调制器的频率温漂对系统稳定性的影响, 以及验证双闭环自适应驱动控制技术的有效性, 采用 632.8 nm 的激光器、基于本课题组研制

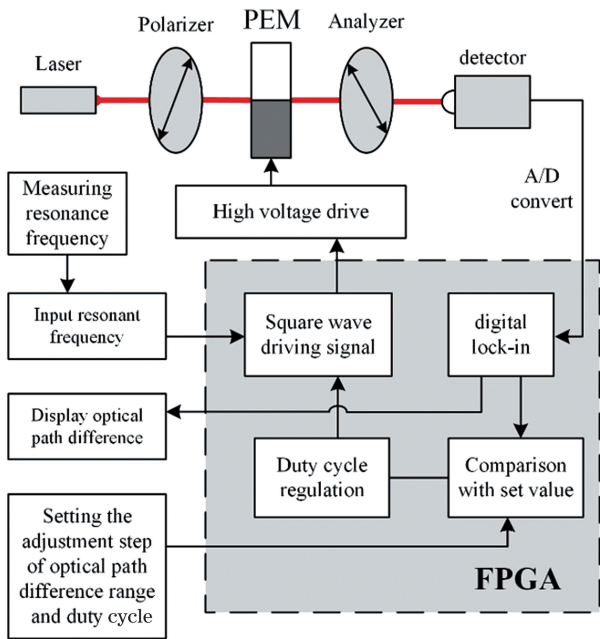


图 6 弹光调制器稳定控制系统流程图

Fig. 6 Flow chart of stability control system of PEM

的弹光调制器、驱动反馈电路、数据处理系统等,搭建了弹光调制器稳定控制系统测试平台,如图 7 所示。

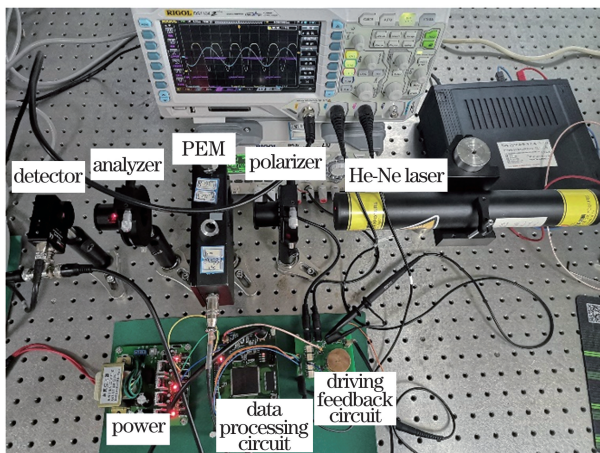


图 7 弹光调制器稳定控制系统测试平台

Fig. 7 Test platform for stability control system of PEM

由于外界温度与弹光调制器的自身热效应会影响其谐振频率的变化,所以实验进行之前需要测出谐振频率。在实验室环境温度约为 25 °C 时,将弹光调制器上电驱动 15 min 后,采用激光多普勒测振仪测量弹光调制器的振动状态,通过 Labview 与 FPGA 通信,控制 DDS 模块在 49.060 ~ 49.120 kHz 的频率范围内,每 0.5 s 增加 0.05 Hz,跟踪  $J_4/J_2$  比值并采集数据,得到的谐振频率如图 8 所示。弹光调制器在谐振频率处光程差最大且  $J_4/J_2$  最大,在当前环境温度下,弹光调制器的谐振

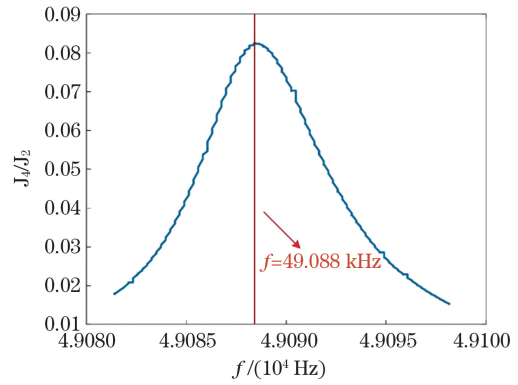
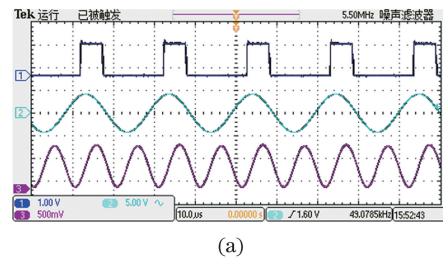


图 8 扫频结果

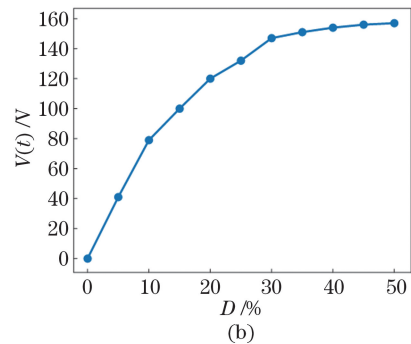
Fig. 8 Frequency sweep result

频率为 49.088 kHz。

接下来,手动调节 DDS 输出的方波信号占空比,占空比在 0% ~ 50% 之间每 5% 记录一次,截取的示波器显示图如图 9(a) 所示,图中 1 通道为驱动方波,通道 2 为驱动电压,通道 3 为干涉调制信号。驱动电压随占空比的变化如图 9(b) 所示。



(a)



(b)

图 9 驱动方波、驱动电压、干涉调制信号波形图,以及占空比与驱动电压的关系图。(a) 驱动方波、驱动电压、干涉调制信号波形图;(b) 占空比与驱动电压的关系图

Fig. 9 Waveforms of driving square wave, driving voltage, and interference modulation signal, and relationship between duty cycle and driving voltage. (a) Waveforms of driving square wave, driving voltage, and interference modulation signal; (b) relationship between duty cycle and driving voltage

根据前述理论推导,当驱动电压随占空比的调

节而变化时,相位调制幅值也会发生相应的变化。在调节过程中:一方面,为了防止反馈调节过量导致占空比单位调节幅度超过相位调制幅值的设定范围,必须保证占空比单位调节幅度足够小且在相位调制幅值设定范围内;另一方面,占空比的调节幅度需要大于温漂后的相位调制幅值波动,以防因调节力度不够而致失控。本测试采用的占空比范围为 30%~40%,每 10 s 增加 0.1% 占空比,干涉信号经 A/D 转换、数字锁相与乘累加运算处理后,将得到的相位调制幅值发送至上位机用于采集存储,得到的数据如图 10 所示。由图 10 可知,1.0% 的占空比对应的  $\delta_0$  为 0.009。

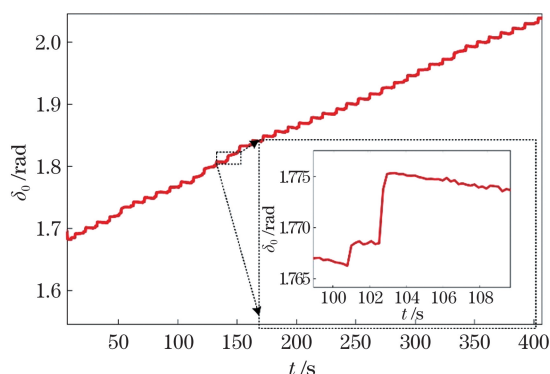


图 10 相位调制幅值图

Fig. 10 Amplitude of phase modulation

通过分析可得无反馈 PEM 的相位调制幅值在平均 5 s 的周期内的变化幅度约为 0.004,因此,在占空比为 0.4%~0.9% 内,取最低允许的调节幅度,以获取尽可能高的准确度,故取调节幅度为 0.0005。

为了验证本控制系统的稳定性,采用半波与 1/4 波状态下的控制结果进行分析。具体测试过程如下:在 FPGA 控制程序中,设置初始频率为弹光调制器的谐振频率 49.088 kHz,设置初始占空比为 35%,设置占空比波动范围为 25%~45% (以防调节过程中,占空比超过 50%,导致驱动电路中全桥部分双桥臂同时导通,从而对芯片及电路造成损害),设置相位调制幅值为半波幅值。弹光调制器的实时调制数据通过串口传到上位机呈现,保存数据,绘制得出相位调制幅值与时间的关系如图 11(a)所示,不加反馈的相位调制幅值与时间的关系如图 11(b)所示。

由图 11(a)与图 11(b)可知,在约 2 h 的反馈控制时长内,半波状态下相位调制幅值最高为 3.15,最低为 3.124,精确度达到 0.82%,而不加反馈的情

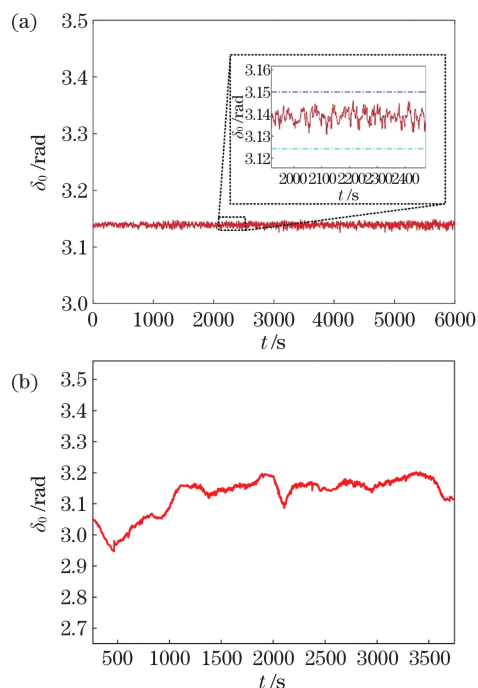


图 11 半波状态下相位调制幅值与时间的关系,以及无反馈的 PEM 相位调制幅值曲线。(a)半波状态下相位调制幅值与时间的关系;(b)无反馈的 PEM 相位调制幅值曲线

Fig. 11 Phase modulation amplitude varying with time at 1/2 wave state, and PEM phase modulation without feedback. (a) Phase modulation amplitude varying with time; (b) PEM phase modulation without feedback

况下,PEM 在整个工作时间内,相位调制幅值出现了多次波动,且波动幅值达到了 0.25。同样地,将相位调制幅值设置为 1/4 波状态,测试结果如图 12 所示,其相位调制幅值最高为 1.574,最低为 1.567,精确度达到 0.44%。

已有的控制方法研究中 PEM 相位调制幅值的

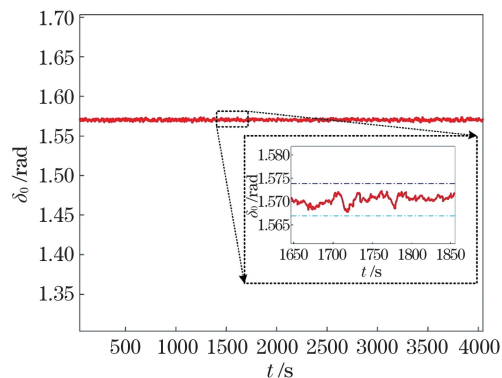


图 12 1/4 波状态下相位调制幅值与时间的变化关系  
Fig. 12 Phase modulation amplitude varying with time at 1/4 wave state

控制精确度如表 1 所示,表中 R 代表交流电调制光信号,DC 代表直流电信号,R/DC fluctuation 用来表示经综合运算处理后光信号与电信号的相位延迟幅值的波动量。相较于无反馈控制的情况,

采取反馈控制后,精确度均有显著提高,温控的方法对于装置要求较高,频率控制不利于后续数据处理,而电压调节没有上述缺陷,且精确度优于上述方法。

表 1 PEM 控制精确度对比

Table 1 Comparison of PEM control accuracy

Method	R/DC fluctuation / %	Reference
Without feedback control	7.90	
Temperature control	1.10	[24]
Driving frequency control	3.30	[25]
Voltage control	0.82	This paper

## 4 结 论

针对弹光调制器工作时谐振频率漂移导致弹光调制器干涉信号的相位调制幅值有较大波动的问题,根据弹光调制器的机械结构,建立了弹光调制器的热交换动态模型,分析了温度对弹光调制器的影响,提出了基于数字锁相技术的占空比闭环控制方法。所提方法与现有的控制方法相比,具有反馈速度快的优点,且精确度与自动化程度都有了相应的提高。搭建了实验系统进行实验验证,结果表明:在半波状态时,弹光调制器的相位调制幅值精确度为 0.82%,在 1/4 波状态时,弹光调制器的相位调制幅值精确度为 0.44%。本研究为分析弹光调制器的工作状态提供了基础,对相位调制幅值控制系统的精确度提升、可靠性评估具有重要的理论指导意义。

## 参 考 文 献

- [1] Bai L F, Wang X, Han J, et al. Development review of new spectral measurement technology[J]. *Infrared and Laser Engineering*, 2019, 48(6): 0603001. 柏连发, 王旭, 韩静, 等. 新型光谱测量技术发展综述[J]. *红外与激光工程*, 2019, 48(6): 0603001.
- [2] Buican T N. Birefringence interferometers for ultra-high-speed FT spectrometry and hyperspectral imaging: I. Dynamic model of the resonant photoelastic modulator [J]. *Vibrational Spectroscopy*, 2006, 42(1): 51-58.
- [3] Luo X W, Wang Z B, Li K W, et al. Design of high voltage driving circuit based on FPGA for photoelastic modulator [J]. *Laser & Infrared*, 2017, 47(10): 1305-1309. 罗欣玮, 王志斌, 李克武, 等. 基于 FPGA 的光弹调制器用高压驱动电路设计[J]. *激光与红外*, 2017, 47(10): 1305-1309.
- [4] Chen G W, An Y Q, Wang Z B, et al. Self tracking technology of photoelastic modulation frequency [J]. *Opto-Electronic Engineering*, 2015, 42(10): 21-26, 32. 陈光威, 安永泉, 王志斌, 等. 弹光调制的频率自跟踪技术[J]. *光电工程*, 2015, 42(10): 21-26, 32.
- [5] Li H X, Lu Y B, Zhu Y F. The guidance of annealing process by stress measurement of ultra-thin float glass [J]. *Glass & Enamel*, 2019, 47(3): 7-11. 李红霞, 路延斌, 朱云峰. 超薄玻璃应力测试及对退火工艺指导[J]. *玻璃与搪瓷*, 2019, 47(3): 7-11.
- [6] Zhang Y H. The study on Herriott photo-elastic modulator [D]. Taiyuan: North University of China, 2015. 张宇寒. Herriott 型的弹光调制干涉具的研究 [D]. 太原: 中北大学, 2015.
- [7] Wei H C. The study of photoelastic modulator and its high-voltage drive technology [D]. Taiyuan: North University of China, 2013: 28-29. 魏海潮. 弹光调制器及其高压驱动技术研究 [D]. 太原: 中北大学, 2013: 28-29.
- [8] Zhang M J, Jing N, Li K W, et al. Thermal stability control system of photo-elastic interferometer in the PEM-FTs [J]. *The Review of Scientific Instruments*, 2018, 89(1): 013105.
- [9] Wang Y C. The research on stability of photoelastic modulation Fourier transform spectrometer [D]. Taiyuan: North University of China, 2014: 26-27. 王艳超. 弹光调制傅里叶变换光谱仪稳定性研究 [D]. 太原: 中北大学, 2014: 26-27.
- [10] Wang Y C, Wang Z B, Zhang J L, et al. Temperature compensation strategy and implementation for photoelectric modulation interferometer with large optical path difference [J]. *Spectroscopy and Spectral Analysis*, 2013, 33(5): 1429-1432. 王艳超, 王志斌, 张记龙, 等. 大光程差弹光调制干涉仪的温度补偿策略及实现 [J]. *光谱学与光谱分析*, 2013, 33(5): 1429-1432.

- [11] Wang B L, List J. Basic optical properties of the photoelastic modulator part I: useful aperture and acceptance angle [J]. *Proceedings of SPIE*, 2005, 5888: 58881I.
- [12] Zeng A J, Wang X Z, Dong Z R, et al. Application of photoelastic modulator in modulation of polarization direction [J]. *Chinese Journal of Lasers*, 2005, 32(8): 1063-1067.  
曾爱军, 王向朝, 董作人, 等. 光弹调制器在偏振方向调制中的应用 [J]. *中国激光*, 2005, 32(8): 1063-1067.
- [13] Zeng A J, Wang X Z, Li D L, et al. A new method to calibrate accurately a photoelastic modulator [J]. *Acta Optica Sinica*, 2005, 25(6): 799-802.  
曾爱军, 王向朝, 李代林, 等. 精确标定光弹调制器的新方法 [J]. *光学学报*, 2005, 25(6): 799-802.
- [14] Hu J M, Zeng A J, Wang X Z. New method for measuring retardation of quarter-wave plate [J]. *Chinese Journal of Lasers*, 2006, 33(5): 659-662.  
胡建明, 曾爱军, 王向朝. 精确测量 1/4 波片相位延迟量的新方法 [J]. *中国激光*, 2006, 33(5): 659-662.
- [15] Hu J M, Zeng A J, Wang X Z. Method to measure phase retardation of wave plate based on photoelastic modulation [J]. *Acta Optica Sinica*, 2006, 26(11): 1681-1686.  
胡建明, 曾爱军, 王向朝. 基于光弹调制技术的波片相位延迟量测量方法 [J]. *光学学报*, 2006, 26(11): 1681-1686.
- [16] Li K W, Wang Z B, Chen Y H, et al. High sensitive measurement of optical rotation based on photo-elastic modulation [J]. *Acta Physica Sinica*, 2015, 64(18): 184206.  
李克武, 王志斌, 陈友华, 等. 基于弹光调制的高灵敏旋光测量 [J]. *物理学报*, 2015, 64(18): 184206.
- [17] Li K W, Wang L M, Wang Z B, et al. Measurement of residual birefringence combined photo-elastic modulation with electro-optic modulation [J]. *Chinese Journal of Lasers*, 2016, 43(5): 0508003.  
李克武, 王黎明, 王志斌, 等. 弹光调制和电光调制联合测剩余双折射 [J]. *中国激光*, 2016, 43(5): 0508003.
- [18] Zhang W, Zhu Q D, Zhang X S. Polarization phase-shifting detection method for central stress in flat glass [J]. *Acta Optica Sinica*, 2018, 38(4): 0426001.  
张伟, 朱秋东, 张旭升. 平板玻璃中部应力的偏振移相检测法 [J]. *光学学报*, 2018, 38(4): 0426001.
- [19] Wang J W, Li K W, Jing N, et al. Phase retardation measurement and fast axis calibration system for wave plate [J]. *Infrared and Laser Engineering*, 2019, 48(2): 0217002.  
王金伟, 李克武, 景宁, 等. 波片相位延迟量测量和快轴标定系统 [J]. *红外与激光工程*, 2019, 48(2): 0217002.
- [20] Wang S, Wang Z B, Li X, et al. Realizing the measurement of the crystal electro-optic coefficient by photoelastic modulation with digital phase locking [J]. *Acta Photonica Sinica*, 2017, 46(10): 1012001.  
王爽, 王志斌, 李晓, 等. 弹光调制测晶体电光系数的数字锁相实现 [J]. *光子学报*, 2017, 46(10): 1012001.
- [21] Zeng A J, Li F Y, Zhu L L, et al. Simultaneous measurement of retardance and fast axis angle of a quarter-wave plate using one photoelastic modulator [J]. *Applied Optics*, 2011, 50(22): 4347-4352.
- [22] Wang N, Wang Y C, Zhang M J, et al. A stability control method of photo-elastic modulator based on voltage compensation [J]. *Laser & Infrared*, 2020, 50(4): 419-424.  
王楠, 王艳超, 张敏娟, 等. 基于电压补偿的弹光调制器稳定性控制方法研究 [J]. *激光与红外*, 2020, 50(4): 419-424.
- [23] Wang N. Research on the key techniques of the micro-birefringence parameters detection [D]. Taiyuan: North University of China, 2020: 26-29.  
王楠. 微小双折射参量检测的关键技术研究 [D]. 太原: 中北大学, 2020: 26-29.
- [24] Hirschy L, Wang B, Wolf J, et al. Basic optical properties of the photoelastic modulator. Part III: thermal properties [J]. *Proceedings of SPIE*, 2012, 8486: 848619.
- [25] Zhang M J, Liu W J, Wang Z B, et al. Study on frequency-drifting characteristics of photo-elastic modulator and stability of Fourier transform spectra [J]. *Infrared and Laser Engineering*, 2020, 49(10): 20200019.  
张敏娟, 刘文敬, 王志斌, 等. 弹光调制器的频率漂移特性及其傅里叶变换光谱的稳定性研究 [J]. *红外与激光工程*, 2020, 49(10): 20200019.

# Photo-Elastic Modulation Based on Adaptive Regulation of Driving Voltage

Liang Zhenkun<sup>1,2,3</sup>, Li Xiao<sup>1</sup>, Wang Zhibin<sup>1,2,3\*</sup>, Li Kewu<sup>1,2,3</sup>, Zang Xiaoyang<sup>1,2,3</sup>

<sup>1</sup>*School of Electrical and Control Engineering, North University of China, Taiyuan, Shanxi 030051, China;*

<sup>2</sup>*Frontier Interdisciplinary Research Institute, North University of China, Taiyuan, Shanxi 030051, China;*

<sup>3</sup>*Nantong Intelligent Optical Electromechanical Research Institute, North University of China, Nantong, Jiangsu 226000, China*

## Abstract

**Objective** With the advantages of high modulation precision, high efficiency, and wide spectral range, photo-elastic modulation technology has attracted considerable attention in many fields, such as optical communication, polarization analysis, and spectral analysis. A series of devices with a photo-elastic modulator as the core are widely used in material detection, scientific research, aerospace, and national defense construction. The basic principle of the photo-elastic modulator is to use the anisotropic crystal of a piezoelectric crystal to provide the external mechanical force, so as to make the photo-elastic crystal produce birefringence. It is a thermal-mechanical-electrical coupling resonant device consisting of photo-elastic and electro-optic crystals. In the working process, the driving circuit provides a high-voltage sine wave signal for the piezoelectric crystal in the vertical direction, making the piezoelectric crystal vibrate horizontally and causing the elastic crystal to deform accordingly, therefore producing periodic birefringence to achieve phase modulation of incident light. The phase modulation amplitude is positively correlated with the voltage amplitude output by the drive circuit. The driving voltage amplitude is positively correlated. When the amplitudes of the driving voltage and phase modulation increase, the piezoelectric quartz and photo-elastic crystal consisting of the photo-elastic modulator will produce thermal loss during mechanical vibration. This will result in the shift of the resonance frequency, making it become a challenge to keep the optical path difference consistent for a long time, which reduces the photo-elastic modulator's stability and modulation efficiency. Besides, the change in the external environment will reduce the modulator's stability. Thus, the stability technology of the photo-elastic modulator plays a significant role.

**Methods** In this study, starting from the structure of the photo-elastic modulator, according to the vibration model of the photo-elastic modulator, the influencing factors of the temperature drift of the photo-elastic modulator are analyzed. The conventional optical system with a photo-elastic modulator as the core is developed. According to the Stokes parameter, Muller matrix, and digital phase-locking technology, the relationship between the driving signal and the phase modulation amplitude is finally obtained, and the correlation function diagram is drawn. Thus, a drive voltage adaptive adjustment method based on a field-programmable gate array (FPGA) is proposed. Direct digital synthesis (DDS) technology is used to control the square wave signal of a photo-elastic modulator. After being amplified by the LC resonant circuit, a high-voltage sine wave is generated to drive the photo-elastic modulator. The incident light is modulated by the photo-elastic modulator and received by the detector. The optical signal is converted into an electrical signal, which is transmitted to FPGA through an analog-to-digital sampling module. By using digital phase-locked technology, we multiply and accumulate the acquisition signal with the quadruple frequency reference signal in the memory to obtain the quadruple frequency correlation component in the acquisition signal, and similarly multiply and accumulate the acquisition signal and the double frequency reference signal to obtain the double frequency correlation component. The relationship between the ratio of the quadruple frequency component to the double frequency component and the phase modulation amplitude is analyzed. The duty cycle is adjusted in real-time according to the ratio of the quadruple and second harmonic frequencies in each cycle. If the ratio obtained in the next cycle is smaller than that in the previous cycle, the duty cycle will increase; otherwise, it will decrease. Finally, the phase modulation amplitude will be stabilized at a fixed range. In the system, two key points need to be determined in advance. One is the resonant frequency of the photo-elastic modulator, and the other is the unit adjustment of the driving square wave duty cycle. Since the external temperature and thermal effect of the photo-elastic modulator affect the change of its resonant frequency, it is essential to determine the resonant frequency of the photo-elastic modulator in the test environment first. The key to the single adjustment of the duty cycle in the



feedback control is that, to prevent excessive feedback regulation, and it is essential to ensure that the duty cycle adjustment amplitude is less than the setting value of the phase modulation amplitude. However, the duty cycle adjustment amplitude should be larger than the fluctuation of the phase amplitude after temperature drift, therefore preventing the lack of control due to the lack of amplitude modulation. At room temperature of 25 °C, the photo-elastic modulator was powered for 15 min. According to the sweep frequency test, the resonant frequency under current temperature is determined. The two tests are conducted to determine the conversion relationship among the duty cycle, driving voltage, and phase modulation amplitude, so as to determine the regulation value of the duty cycle unit.

**Results and Discussions** The stability of the system is tested by experiments. Compared with the previous studies (Table 1), the accuracy has been significantly improved. When the incident light wavelength is 632.8 nm, the phase modulation amplitude accuracy is 0.82% at the half-wave state and 0.44% at the quarter-wave state [Fig. 11 (a) and Fig. 12]. The constant temperature control method is more stringent for the device and environment. The frequency control method is not conducive for data processing after application. The voltage regulation has none of the above shortcomings, and the accuracy is higher than that of the above two methods.

**Conclusions** Based on the temperature drift model and digital phase-locked technology, the phase modulation amplitude stability control of the photo-elastic modulator is realized. The experimental results show that the voltage self-regulation method has higher accuracy, a wide application range, and more convenient for subsequent data processing than the existing temperature control and frequency regulation methods. It has important theoretical significance for improving the accuracy and reliability evaluation of phase modulation amplitude control system.

**Key words** measurement; phase modulation; photo-elastic modulator; digital phase-locked technology; temperature drift model; feedback control

**OCIS codes** 120.5060; 130.4110; 160.1190